Phase Conversion of Ice-Templated α-Tricalcium Phosphate Scaffolds into Low-Temperature Calcium Phosphates with Anisotropic Open Porosity

*Annika Seifert, Jürgen Groll, Jan Weichhold, Anne V. Boehm, Frank A. Müller, and Uwe Gbureck**

The current study aims to extend the material platform for anisotropically structured calcium phosphates to low-temperature phases such as calcium-deficient hydroxyapatite (CDHA) or the secondary phosphates monetite and brushite. This is achieved by the phase conversion of highly porous α-tricalcium phosphate (α-TCP) scaffolds fabricated by ice-templating into the aforementioned phases by hydrothermal treatment or incubation in phosphoric acid. Prior to these steps, α-TCP scaffolds are either sintered for 8 h at 1400 °C or remain in their original state. Both nonsintered and sintered α-TCP specimens are converted into CDHA by hydrothermal treatment, while a transformation into monetite and brushite is achieved by incubation in phosphoric acid. Hydrothermal treatment for 72 h at 175 °C increases the porosity in nonsintered samples from 85% to 88% and from 75% to 88% in the sintered ones. An increase in the specific surface area from (1.102 ± 0.005) to (9.17 ± 0.01) m^2 g^{-1} and from (0.190 ± 0.004) to (2.809 ± 0.002) m^2 g^{-1} due to the phase conversion is visible for both the nonsintered and sintered samples. Compressive strength of the nonsintered samples increases significantly from (0.76 ± 0.11) to (5.29 ± 0.94) MPa due to incubation in phosphoric acid.

1. Introduction

While bone is a hierarchically structured tissue with an anisotropic orientation of the building blocks on different length scales,[1–3] most bone replacement materials based on calcium phosphate ceramics only feature an isotropic distribution of their pore network. These interconnecting pores are intended to enable cell infiltration, interaction with adjacent tissues and vascularization, which is indispensable for the successful implantation.[4] The formation and ingrowth of newly formed bone into the implant is enhanced by the use of highly porous scaffolds. The pore size considered ideal depends on the clinical application, but should be at least 100 μm.[5,6] However, only a few bone graft substitute examples are known in which hierarchical and ordered pore designs are used. These unidirectional structures cause a more rapid cell ingrowth,[7] improved nutrient supply, and vascularization capabilities in the preferred pore direction.[8] Such scaffolds can, for instance, be fabricated with the aid of additive manufacturing techniques such as 3D powder printing or dispense plotting.[9–17] However, these methods are only suitable for the fabrication of pores in the order of more than a few hundred microns. A promising approach to achieve an ordered lamellar structure with precisely adjustable pore sizes below 100 μm and a specifically modified pore orientation is directional freezing.[18] Here, a ceramic slurry is frozen in the presence of an external temperature gradient. The growing ice lamellae expel all components of the slurry and accumulate them between the ice crystals. By removing the ice crystals through freeze-drying, a porous scaffold with highly aligned pores is created, which represents a negative of the ice crystal structure.[19] This process is currently limited to high-temperature calcium phosphates (CaP) such as hydroxyapatite[20] (HA) or tricalcium phosphate (TCP).[21] However, these microcrystalline high-temperature CaPs only dissolve poorly at physiological pH and have a lower absorption rate in vivo than low-temperature CaPs, such as calcium-deficient hydroxyapatite (CDHA, $Ca_9(PO_4)_5(HPO_4)OH$), brushite ($CaHPO_4 \cdot 2H_2O$), or monetite ($CaHPO_4$).[22,23] CDHA, for example, is nanocrystalline with a high specific surface area,

A. Seifert, Prof. J. Groll, J. Weichhold, Prof. U. Gbureck
Department for Functional Materials in Medicine and Dentistry at the Institute of Functional Materials and Biofabrication
University of Würzburg
Pleicherwall 2, D-97070 Würzburg, Germany
E-mail: uwe.gbureck@fmz.uni-wuerzburg.de

A. V. Boehm, Prof. F. A. Müller
Otto Schott Institute of Materials Research (OSIM)
Friedrich Schiller University Jena
Löbdergraben 32, D-07743 Jena, Germany

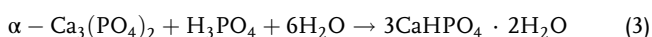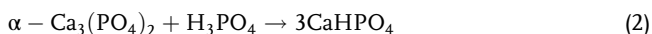The ORCID identification number(s) for the author(s) of this article can be found under https://doi.org/10.1002/adem.202001417.

which, in turn, is supposed to improve the biological performance of the implant.[22] Although brushite and monetite are usually microcrystalline, their higher solubility when compared with secondary calcium phosphates leads to faster resorption and bone regeneration in vivo.[24]

The current study aims to expand the material platform for ice-templated and highly porous calcium phosphate ceramics to the low-temperature phases such as CDHA, brushite, and monetite. This was achieved by structuring α-TCP into highly porous scaffolds, which were subsequently converted by hydrothermal treatment[25] or by incubation in phosphoric acid.[26] Hydrothermal treatment initiates a cement reaction of α-TCP and water, which, according to Equation (1), results in CDHA as the end product[27]

$$3\alpha - Ca_3(PO_4)_2 + H_2O \rightarrow Ca_9(PO_4)_5(HPO_4)OH \qquad (1)$$
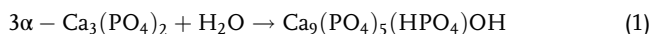
Incubation in phosphoric acid converts α-TCP to monetite or brushite using Equation (2) and (3), respectively.

$$\alpha - Ca_3(PO_4)_2 + H_3PO_4 \rightarrow 3CaHPO_4 \qquad (2)$$

$$\alpha - Ca_3(PO_4)_2 + H_3PO_4 + 6H_2O \rightarrow 3CaHPO_4 \cdot 2H_2O \qquad (3)$$

Here, different processing parameters such as duration and temperature of the hydrothermal treatments were systematically varied and their influence on sample morphology, phase composition, and mechanical properties of the resulting scaffolds was investigated. The latter are thought to have a high clinical potential due to the higher solubility of the obtained calcium phosphate phases, which will, in turn, accelerate bone regeneration.

2. Results

2.1. Phase Composition

The phase transformation of α-TCP induced by the different post-treatments was analyzed by X-ray diffractometry (XRD) measurements (**Figure 1**). During the hydrothermal treatment at 117 °C it was observed for both sample types, i.e., nonsintered and sintered, that a partial phase transformation from α-TCP to β-TCP, CDHA, and, in addition, monetite in the nonsintered samples occurred (Figure 1a,b and **2**). While monetite appeared as a transition phase, a complete phase transformation to CDHA was found in both cases after hydrothermal treatment for at least 48 h (Figure 1c,d and 2).

Treatment in phosphoric acid solution led to a partial recrystallization of α-TCP into monetite for the nonsintered samples and into β-TCP and highly crystalline brushite for the sintered ones (Figure 1 and 2).

Furthermore, the crystallite size was determined, as shown in **Table 1** (n.c. = not calculable; either the crystallite size was too low <10 nm or too high >1000 nm).

It can be seen that the crystallite sizes increase with the sintering process. During sintering, the small precipitated crystals fuse into a larger crystallite due to solid diffusion.

2.2. Morphological Changes

Structural changes that occurred during the hydrothermal or acidic treatment of the nonsintered α-TCP samples were visualized by scanning electron microscopy (SEM) (**Figure 3**). After the freeze-drying of the specimens it became apparent that the pores were arranged parallel to each other in a highly ordered manner. The lamellae between the pores consisted of α-TCP crystals and alginate (Figure 3a). Due to the hydrothermal treatment at 117 °C for 3 h, the morphology of the lamellae changed. Here, fine CDHA needles or whiskers appeared, which originated in the lamellae and partially protruded into the pores (Figure 3b). These needle-like structures were also visible after 8 h of hydrothermal treatment (Figure 3c). A closer look at one selected lamella showed that the CDHA whiskers were arranged in tufts and distributed over the entire lamella (Figure 3g). This structure did not change significantly by hydrothermal treatment at higher temperatures and longer durations (Figure 3d,e). The only notable difference was that the needles seemed to become slightly thicker (Figure 3h).

An apparently different morphology could be observed after incubation in phosphoric acid. Small platelet-shaped monetite crystals emerged from the lamellae, grew into the pores, and filled them nearly completely in a still porous manner (Figure 3f,i).

The remaining samples were sintered after freeze-drying and subjected to hydrothermal or acidic treatment afterward. After the sintering process, without any treatment step, the aligned pore structure was preserved. The lamella surfaces were smooth without individual crystals being visible (**Figure 4**a). After the treatment at 117 °C for 3 h, the plain surface changed. Both platelet-shaped and needle- or rod-like CDHA crystals, which protruded into the pores, were visible (Figure 4b). This structure also occurred after 8 h (Figure 4c,g). A more detailed examination of the structure showed that the CDHA needles were thicker, flatter, and longer than in the nonsintered scaffolds. Due to the hydrothermal treatment at 175 °C, the platelet-shaped crystals disappeared (Figure 4d). In addition, the needles became shorter and were increasingly located on the lamellae. It could also be shown that, especially with long treatment times, CDHA needles became shorter, arranged parallel to each other, and formed bundles. The size of these bundles was in the order of several micrometers (Figure 4e,h). However, crystal length was examined in a separate investigation, as shown in **Figure 5**.

Due to the incubation in phosphoric acid, a distinct structural change occurred. While the pores were still aligned, a complete transformation of the smooth lamellar structure was observed. Small brushite crystals appeared, which did not protrude into the pores, but were localized on the lamellae (Figure 4f). These crystals also tended to be arranged in bundles (Figure 4i).

A comparison of the CDHA needles of nonsintered and sintered samples obtained by incubation at 117 °C for 8 h (Figure 3g and Figure 4g) shows that the needles of nonsintered samples were thinner and shorter than those of the sintered ones. These were flatter, broader, and sturdier.

A quantitative evaluation of the length of crystals growing into the pores after hydrothermal treatment at 175 °C (both sample types were treated in demineralized water vapor at this
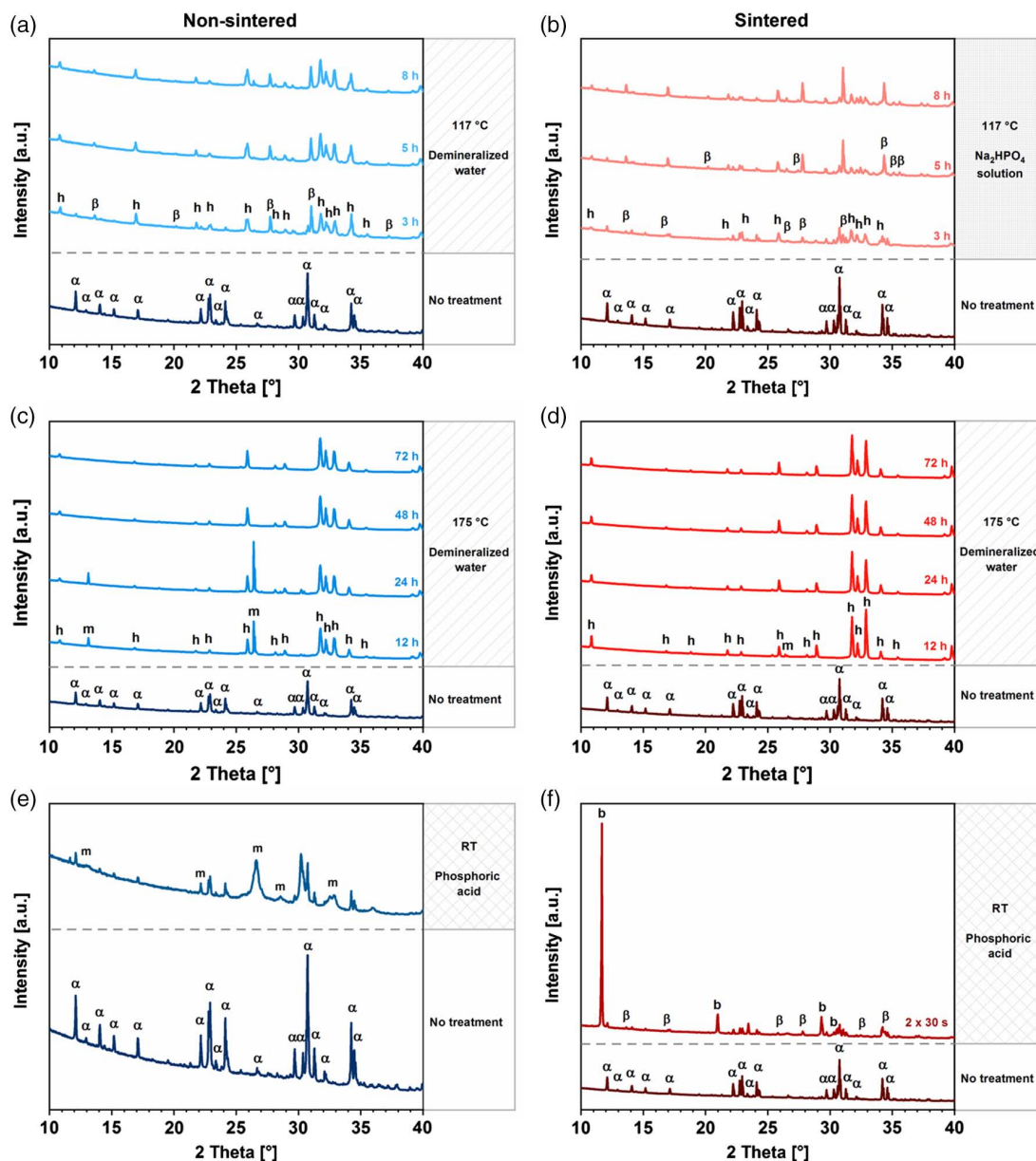
Figure 1. XRD patterns of nonsintered and sintered specimens. In the left column, XRD measurements of the nonsintered samples are shown in shades of blue, while those of the sintered samples are shown in red in the right column. The XRD spectra in the different rows are sorted by treatment, i.e., hydrothermal treatment at a,b) 117 °C (upper row), c,d) 175 °C (middle row), and e,f) incubation in phosphoric acid solution (lower row). The intensity maxima for (α) α-TCP, (β) β-TCP, (h) CDHA, (m) monetite, and (b) brushite are indicated.

temperature) is shown in Figure 5a. Needles in the nonsintered specimens were between 9 and 11 times shorter than those in the sintered ones. A reduction in crystal length in the nonsintered samples was found after 24 h, while it increased again after 48 and 72 h. In the sintered samples, a significant ($p < 0.001$) increase was observed only after 72 h of hydrothermal treatment.

Figure 5b shows the length of CDHA crystals within the bundles formed in the sintered samples during incubation at 175 °C. These became significantly ($p < 0.001$) shorter after 72 h incubation time and decreased by a factor of approximately 2.5.

2.3. Pore Size Distribution and Porosity

Pore size distribution, relative pore volume, and porosity were measured by mercury porosimetry. Although the widely used characterization method of microcomputed tomography (μ-CT) offers several advantages, such as nondestructive measurement and detection of both closed and open pores, the main benefit of mercury intrusion is the detection of accessible pores down to a size of 0.0036 μm (according to the manufacturer's information, see Experimental Section). Compared with μ-CT with a detection limit of 1 μm,[28] this resolution is thus significantly higher.
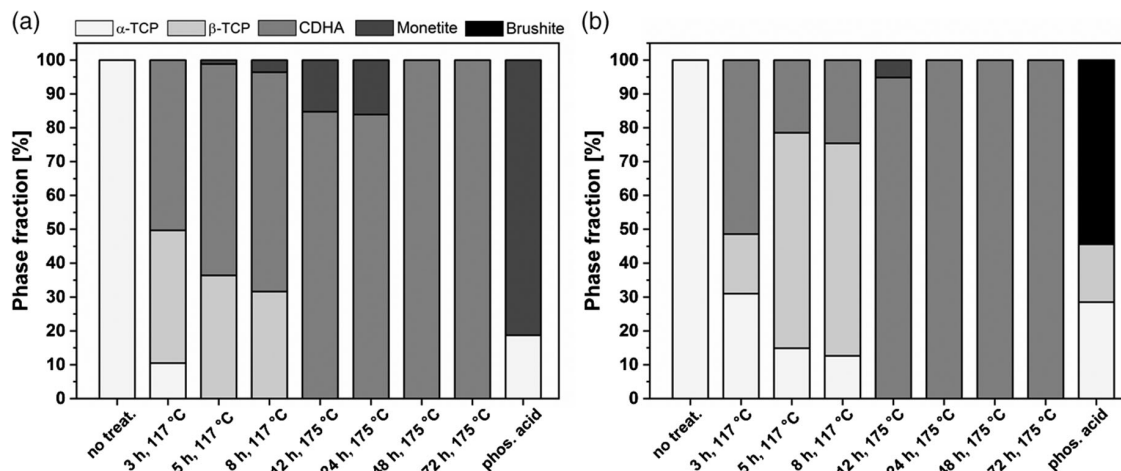
ADVANCED
SCIENCE NEWS
www.advancedsciencenews.com

ADVANCED
ENGINEERING
MATERIALS
www.aem-journal.com

Figure 2. Changes in phase composition due to different treatment types. a) Nonsintered samples: with increasing incubation time and temperature of the hydrothermal treatment, α-TCP converted completely to CDHA after 48 h via the intermediate phases β-TCP and monetite. Incubation in phosphoric acid solution caused a partial conversion to monetite. b) Sintered samples: with increasing incubation time and temperature of the hydrothermal treatment, α-TCP converted completely to CDHA after 24 h via the intermediate phases β-TCP and monetite. Incubation in phosphoric acid solution caused a partial conversion to β-TCP and brushite.

Table 1. Crystallite size in dependence of different treatments.

Treatment		Crystallite size [nm]				
		α-TCP	β-TCP	CDHA	Monetite	Brushite
No treatment	Nonsintered	359	–	–	–	–
	Sintered	n.c.	–	–	–	–
8 h, 117 °C	Nonsintered	–	249	88	249	–
	Sintered	n.c.	541	135		–
72 h, 175 °C	Nonsintered	–	–	119	–	–
	Sintered	–	–	319	–	
2 × 30 s, phosphoric acid solution	Nonsintered	n.c.	–	–	40	–
	Sintered	n.c.	n.c.	–		n.c.

The effects of hydrothermal and acidic treatment on pore size distribution, specific volume, and porosity are shown in **Figure 6**. For the purpose of better clarity, only the pore size distributions without treatment, after 8 h at 117 °C, after 72 h at 175 °C, and after incubation in phosphoric acid, were presented in an exemplary manner.

Considering the nonsintered samples, a nearly monomodal narrow pore size distribution with a maximum of 23 μm was revealed without treatment (Figure 6a). Due to hydrothermal treatment at 117 °C, this distribution widened especially to smaller pore sizes and also the maximum shifted slightly in this direction to 9 μm (Figure 6c). After 72 h at 175 °C, this maximum was increased again and shifted to a size of 16 μm (Figure 6e). A trimodal pore size distribution could be observed after the treatment in phosphoric acid solution (Figure 6g). Total porosity decreased from 85% to 82% after the treatment for 8 h at 117 °C and increased again to a value of 88% due to the treatment for 72 h at 175 °C. The porosity decreased to a value of 79% by incubation in phosphoric acid solution (Figure 6a,c,e,g).

The overall porosity of sintered samples was lower than that of the nonsintered ones. However, a similar trend could be observed. Here, the porosity increased from 75% to 77% and 88% due to the treatment for 8 h at 117 °C and 72 h at 175 °C, respectively, and dropped to 59% due to acidic treatment (Figure 6b,d,f,h). The pore size distribution showed a monomodal distribution for both untreated and hydrothermally treated samples. Here, the maximum ranged between 23 and 11 μm. After incubation in phosphoric acid solution, the distribution spread again to smaller pores. The maximum was reduced to one-third, i.e., 3 μm (Figure 6h).

2.4. Specific Surface Area

The specific Brunauer–Emmett–Teller (BET) surface area is shown in **Figure 7**. An increase in the specific surface area from (1.102 ± 0.005) to (9.17 ± 0.01) $m^2\,g^{-1}$ and from (0.190 ± 0.004) to (2.809 ± 0.0022) $m^2\,g^{-1}$ due to hydrothermal treatment for 5 h at 117 °C is visible for both the nonsintered and sintered samples, respectively.
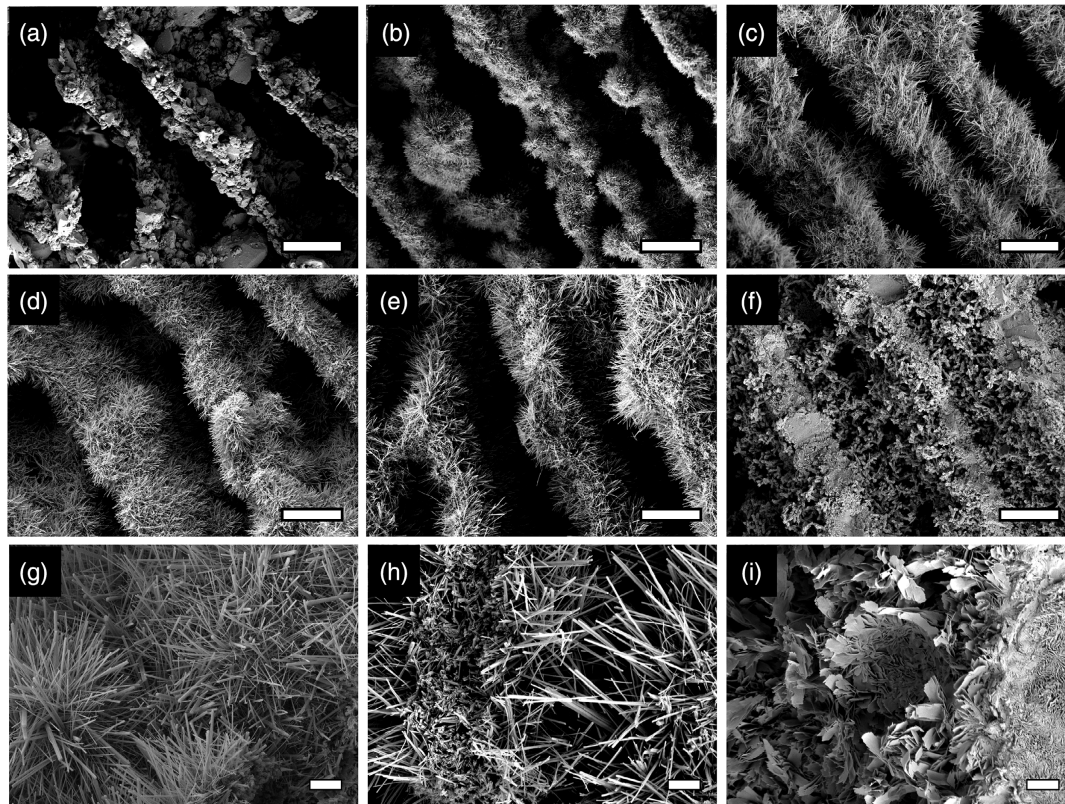
Figure 3. Influence of hydrothermal and acidic treatment on the morphology of nonsintered specimens. a) Highly ordered pores in a freeze-structured sample after freeze-drying. α-TCP crystals could be observed on the lamellae. b,c) Due to hydrothermal treatment at 117 °C for 3 and 8 h, respectively, fine CDHA whiskers grew on the lamellae. The structure was similar d) after incubation for 12 h at 175 °C and e) 72 h at 175 °C. f) After incubation in phosphoric acid solution, platelet-shaped monetite crystals grew into the pores. g) Magnification of a selected lamella after 8 h at 117 °C. Fine CDHA needles were arranged in tufts. h) This was also visible after 72 h at 175 °C. i) Magnification of crystals resulting from incubation in phosphoric acid solution. Scale bars are 15 μm in the two top rows (a–f) and 2 μm in the lower row (g–i).

2.5. Mechanical Properties

The influence of hydrothermal and acidic treatment on the mechanical properties was investigated by compressive strength tests (**Figure 8**).

While the compressive strength of nonsintered samples did not change considerably after 3 and 5 h of hydrothermal treatment at 117 °C and was slightly below 1 MPa, it increased significantly ($p < 0.001$) to (1.60 ± 0.11) MPa after 8 h. After hydrothermal treatment at 175 °C, the compressive strength dropped again to (0.51 ± 0.31) MPa after 72 h but remained at a similar level for all treatment durations. Due to incubation in phosphoric acid solution, a significant increase to (5.29 ± 0.94) MPa was observed (Figure 8a).

This value is comparable to the compressive strength of sintered samples (Figure 8b). During the treatment of these samples at 117 °C in disodium hydrogen phosphate (Na_2HPO_4) solution, the values remained approximately constant. After hydrothermal treatment at 175 °C, compressive strength decreased significantly ($p < 0.001$) to values around 2 MPa, whereby the incubation time had no influence on the compressive strength. Also, due to incubation in phosphoric acid solution, the compressive strength remained within this range.

3. Discussion

The aim of this study was to extend the material field for freeze-structured and highly porous calcium phosphate ceramics with anisotropic pores from high-temperature ceramics to the low-temperature phases CDHA, brushite, and monetite. The principle of directional solidification has been known for a very long time and is widely used as it is one of the most important steps in the metal casting process.[29] In addition to such high-temperature applications, the use of low-temperature processes, i.e., the controlled freezing of aqueous solutions, is also widespread. Therefore, freeze-structuring of a variety of materials is being investigated for applications in various other areas, ranging from research on novel battery applications,[30] thermal energy storage,[31] and cryopreservation of cells[32] to the fabrication of hierarchically structured biomaterials.[33] Advantages of a directional pore structure for biomaterials include enhanced cell migration[7] and facilitation of vascularization.[8] In addition, a much higher loading capacity can be observed along the z-axis, i.e., in the freezing direction, compared with the direction perpendicular to pore orientation.[34] The directional pores can also be adjusted in their properties, for example, their diameter or orientation, by selecting suitable freezing parameters, such as
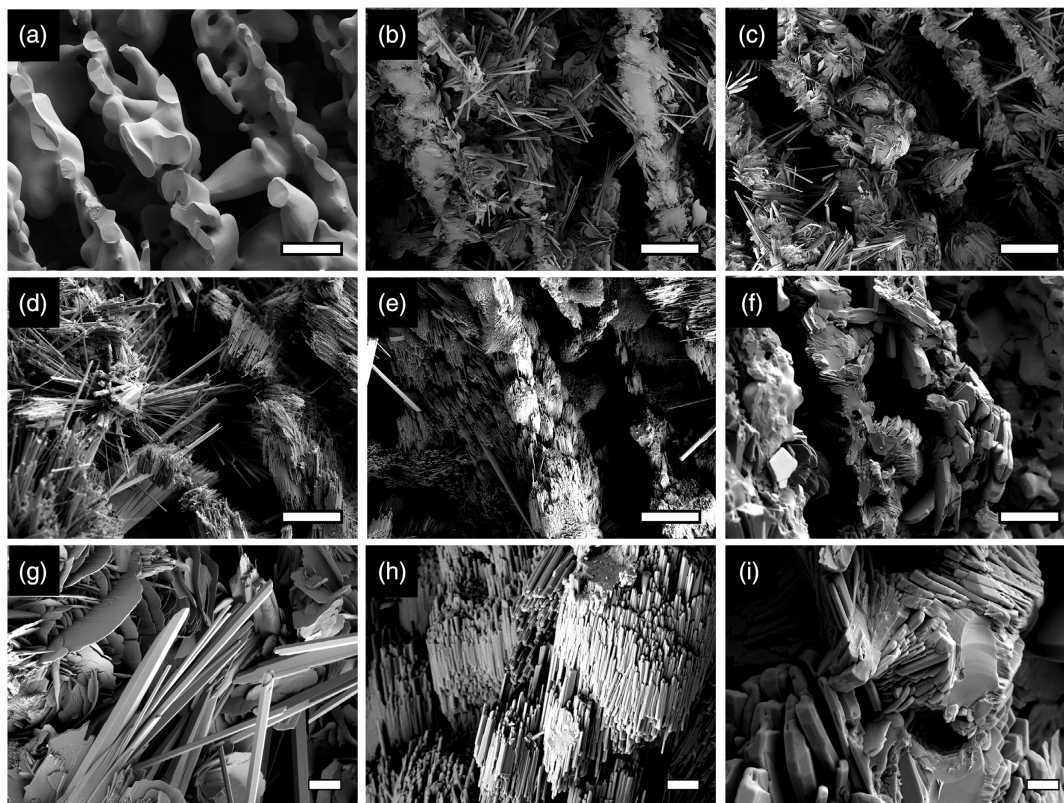
Figure 4. Influence of hydrothermal and acidic treatment on the morphology of sintered specimens. a) Highly ordered pores in a freeze-structured sample after sintering with a smooth lamella surface. b,c) Due to hydrothermal treatment at 117 °C for 3 and 8 h, respectively, platelet-shaped and needle-like CDHA crystals, which protruded into the pores, appeared. During incubation for d) 12 h at 175 °C and e) 72 h at 175 °C, bundles of CDHA crystals were formed. f) Due to incubation in phosphoric acid solution, small brushite crystals developed. g) Magnification of a selected lamella after 8 h at 117 °C. CDHA crystals were flat and long. h) Magnification of CDHA needle bundles, which were formed after 72 h at 175 °C. i) Magnification of brushite crystals resulting from incubation in phosphoric acid solution, which also tended to be arranged in bundles. Scale bars are 15 μm in the two top rows (a–f) and 2 μm in the lower row (g–i).
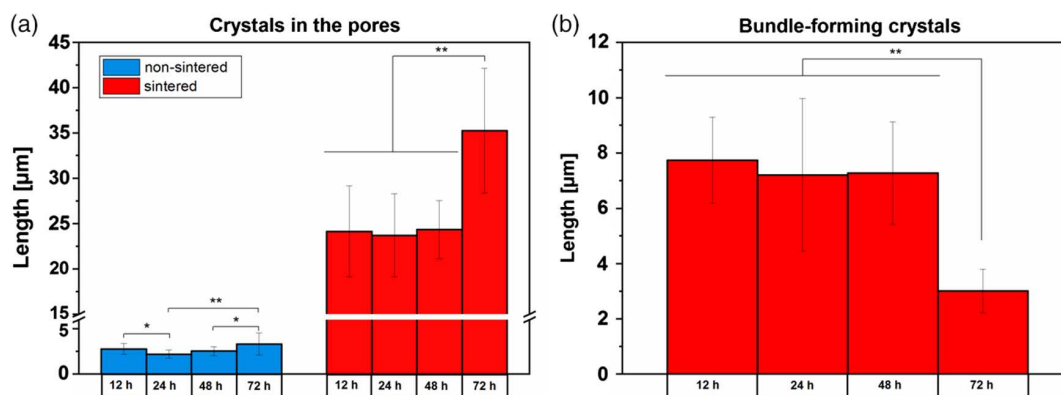

Figure 5. Effect of incubation time on CDHA crystal length due to hydrothermal treatment at 175 °C. a) Length of CDHA crystals growing into the pores. Needle-like crystals of the nonsintered samples were shorter than those of sintered ones. The length increased for sintered samples with increasing incubation time. The crystal lengths of nonsintered samples are shown in blue, those of sintered samples in red. b) Influence of incubation time on the length of bundle-forming crystals in the sintered samples. These became shorter with increasing incubation time (mean $\pm$ SD, $n = 25$, $*p < 0.05$, $**p < 0.001$).

the magnitude of the external temperature gradient.[18] An important biomaterial application of such freeze-structured scaffolds is bone replacement, where (apart from the gold-standard autologous bone transplantation) usually porous calcium phosphate ceramics with isotropic pore orientation[35,36] are used to fill a defect. More recently, freeze-structured ceramic scaffolds
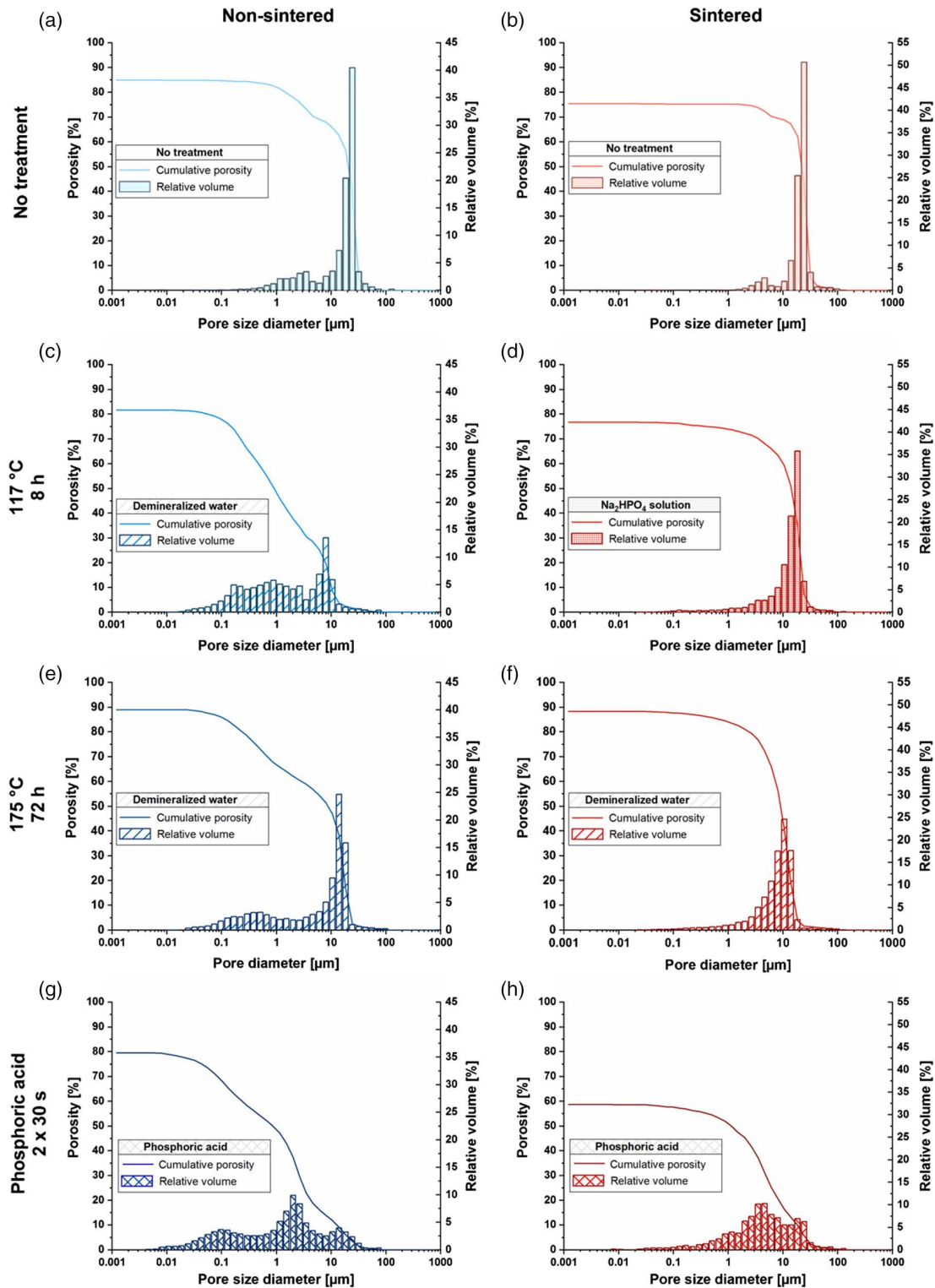
Figure 6. Pore size distribution, relative volume, and porosity of nonsintered and sintered samples before and after different treatments. In the left column, measurements of the nonsintered samples are shown in shades of blue, while those of the sintered samples are shown in red in the right column. The rows indicate the treatment type. From top to bottom: a,b) no treatment, c,d) hydrothermal treatment for 8 h at 117 °C, e,f) hydrothermal treatment for 72 h at 175 °C, and g,h) incubation in phosphoric acid solution. Both the nonsintered and sintered samples showed a monomodal pore size distribution with a maximum at 23 μm for both sample types without treatment. The different treatments shifted this maximum to lower values. Porosity ranged from 79% (incubation in phosphoric acid solution (g)) to 88% (hydrothermal treatment for 72 h at 175 °C) for the nonsintered samples and from 59% (incubation in phosphoric acid solution (h)) to 88% (hydrothermal treatment for 72 h at 175 °C) for the sintered samples.
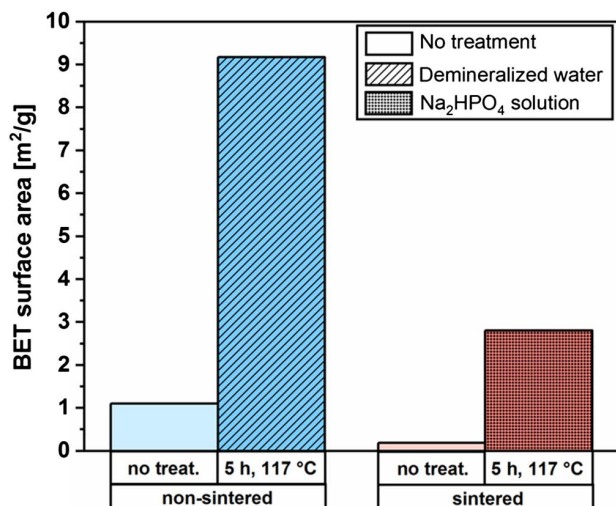
Figure 7. Specific BET surface area. The lighter blue bar corresponds to a nonsintered sample without treatment, darker blue to a nonsintered sample treated for 5 h at 117 °C. The respective equivalents for sintered samples are shown in shades of red.

Therefore, incubation in acidic phosphate solution was chosen for the conversion of reactive α-TCP[42] into brushite and monetite, while α-TCP scaffolds were hydrothermally treated in water vapor at nearly pH neutral conditions for a conversion into CDHA. By using this reactive system, it was possible to produce both nonsintered and sintered scaffolds after freeze-structuring, which were subsequently converted into the aforementioned low-temperature phases without affecting the highly ordered, directional pore structure. This is shown by the SEM images for both the nonsintered (Figure 3) and the sintered samples (Figure 4). The idea of first fabricating the scaffold in its final structure and shape and then converting it into a low-temperature calcium phosphate by a cement reaction was already realized by Galea et al.[25,26] However, these samples did not exhibit ordered porosity.

In nonsintered samples, hydrothermal treatment resulted in the transformation of α-TCP crystals into tuft-like, fine CDHA needles without affecting the overall scaffold porosity. This is demonstrated by considering the phase composition determined by the corresponding XRD measurements (Figure 1), in which the CDHA content ranged between 50% and 100% (Figure 2). This is consistent with previous studies which showed that the cement reaction caused by hydrothermal treatment led to the precipitation of CDHA in the form of fine needles.[43] After hydrothermal treatment of sintered samples, HA needles were also found, but these were considerably thicker than the fine needles in nonsintered samples, leading to an increase in porosity from 75% to 88% after 72 h at 175 °C (Figure 6). This is even higher than the porosity achieved by particle leaching from CDHA cements, which reached porosities of up to 81% and open macropores of 400–500 μm in size.[44] Such formation of rod-shaped HA crystals under hydrothermal treatment, especially in the presence of vapor[45] or in Na_2HPO_4 solution,[46] has previously been observed in other studies and confirms our observations. However, it was remarkable that at a treatment temperature of 175 °C, bundles of HA needles were formed in the sintered samples, which was also found
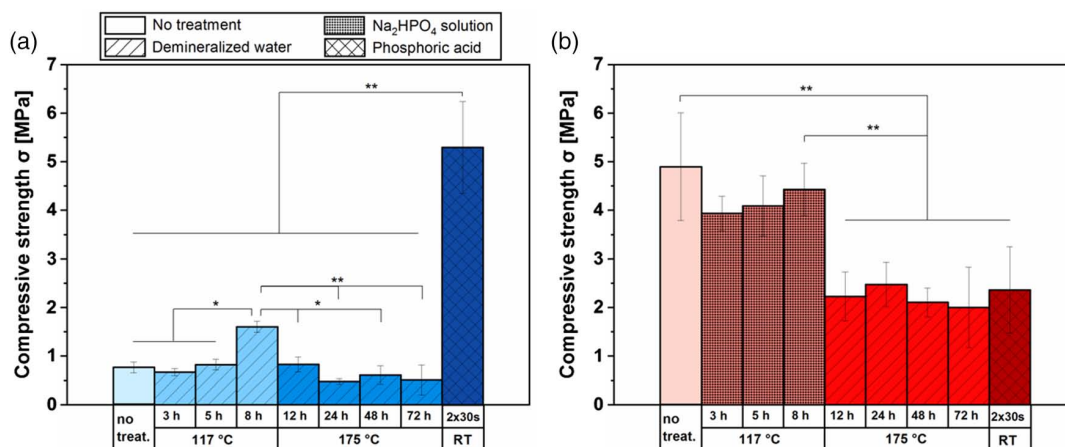
consisting of sintered HA[20,37–40] or β-TCP[21] have been presented as a novel approach for bone tissue engineering. However, such high-temperature phases have slow resorption kinetics and would therefore only lead to a long-term defect regeneration. Here, an improvement in terms of regeneration speed could be achieved by using either nanocrystalline HA or secondary calcium phosphates such as brushite or monetite. As these phases are only stable at low temperature, the fabrication process has to be adequately designed to achieve sufficient mechanical stability while avoiding a final sintering regime. In the current study, this was achieved by ice-templating of α-TCP slurries with a subsequent phase transformation into various low-temperature CaPs, by taking advantage of the different stabilities of calcium phosphates depending on the pH value.[41]

Figure 8. Influence of hydrothermal and acidic treatment on the compressive strength. a) Nonsintered samples: compressive strength without treatment is shown in light blue; strengths after hydrothermal treatment at 117 and 175 °C and after incubation in phosphoric acid are represented in darker shades of blue. b) Sintered samples: compressive strength without treatment is shown in light red; strengths after hydrothermal treatment at 117 and 175 °C and after incubation in phosphoric acid are represented in darker shades of red (mean ± SD, $n = 5$, *$p < 0.05$, **$p < 0.001$).

in sintered α-TCP blocks,[25] whereas this phenomenon could not be observed in nonsintered samples.

Nanocrystalline HA is structurally very similar to the inorganic component in bone.[47–49] Due to its nanocrystallinity, it has a much higher specific surface area, which leads to an increased kinetic solubility.[50] Our results show that the specific surface area of the nonsintered samples was increased eightfold by the conversion of α-TCP into CDHA, caused by the formation of fine whiskers. Similar findings were observed for the sintered samples, where the specific surface area was even increased by a factor of 15 due to the growth of rod- and platelet-shaped CDHA crystals (Figure 7).

Another low-temperature approach for the preparation of CDHA nanocomposites was described by Kniep et al.,[51–55] whose group investigated the process of biomineralization on the model system gelatin-fluorapatite. Here, gelatin was mineralized using a double diffusion technique. Solutions containing calcium and phosphate ions were located in two different reservoirs and migrated into a gelatin gel, which was located in between. This led to the formation of gelatin–apatite nanocomposites. Drawbacks of this process include the sensitive dependence on the materials used and the limited material spectrum. This issue is not present in our samples because the reactive α-TCP system can be converted into the selected material by a cement reaction through suitable post-treatment steps. Here, the previously mentioned advantages of an aligned pore structure were combined with the benefits of using the low-temperature calcium phosphates CDHA, brushite, and monetite.

Incubation of ice-templated samples in phosphoric acid solution resulted in a conversion to the secondary phosphates such as monetite and brushite. Both minerals are often used as materials in bone replacement applications due to their high resorption rate under physiological conditions, which makes them highly interesting for medical treatments.[24,56–58] Immersion of the nonsintered samples in phosphoric acid solution resulted in a phase transformation to monetite with a platelet-shaped, microcrystalline crystal structure growing into the pores. In contrast, the sintered samples transformed into brushite crystals, which tended to form bundles. Brushite usually crystallizes in different morphologies depending on the growth conditions. Abbona et al. reported that often several crystal types were found at the same time, but depending on the concentration, at low pH and 25 °C, flat tabular crystals were more frequently observed.[59] These can also be seen in the SEM images of the brushite samples from our study (Figure 4f,i).

For conventionally prepared, nonstructured brushite cements with a powder-to-liquid ratio of 1 g mL^{-1}, Sheik et al. reported a porosity of 65% and a bimodal pore size distribution with modal values of 4 and 9 μm. If these cements were converted into monetite by autoclaving or dry heating, porosities of 60% and pore sizes of about 5–8 and 3–8 μm, respectively, could be achieved.[60] When comparing these values with the parameters determined by us, it is noticeable that the brushite samples had a slightly lower porosity of 59%, which was due to the crystal ingrowth into the pores. The pore sizes were in a similar range, whereby also pores much larger than 10 μm were observed in our samples. For monetite cements, clearly higher porosities (almost 80%) were achieved by freeze-structuring, with the advantage of aligned pores in the entire sample (Figure 6). Another study that investigated brushite cements

with a powder-to-liquid ratio of 2 g mL^{-1} reported a total porosity of around 70% after the storage of the specimens in phosphate buffered saline for 24 h. After conversion to monetite through autoclaving, the porosity measured nearly 72%.[61]

All scaffolds presented in this study were highly porous, especially after conversion to CDHA by hydrothermal treatment for 72 h at 175 °C, where a porosity of 88% could be achieved (Figure 6). Such high porosities are beneficial in terms of the ingrowth of newly formed bone.[5] As the minimum pore size for bone graft substitutes is regarded as 100 μm,[6] pore diameters of the scaffolds presented in this study are below this value. Nevertheless, larger pores could be realized with only minor effort, e.g., by adjusting the freezing parameters[18] or using a lower powder-to-liquid ratio: the more water available in the slurry, the more ice is formed during the freezing process, resulting in larger pores after lyophilization.

In addition to properties such as architecture, structure, and phase composition of a scaffold, the mechanical properties of a bone replacement material are of crucial importance. Even if the scaffold is to be used in nonload-bearing areas, it must be stable enough to allow handling during surgery, which should be given at a strength of a few MPa.

A comparison of the porosity-dependent compressive strengths determined in our study with previously found values[44,60,61] is shown in **Figure 9**. Despite the lower porosity, the strength of our brushite specimens was below the values found in the literature.[60,61] In contrast, the monetite samples presented in our study exhibited a higher porosity of almost 80% and a higher or comparable compressive strength. In addition, the CDHA samples showed comparable or improved properties compared with results reported in previous studies.[44]

It can be concluded that despite the high porosity, which was around 90% for certain specimens in the presented study (Figure 6), the compressive strength of all samples was between about 1 and 5 MPa. Compared with human cortical bone, which
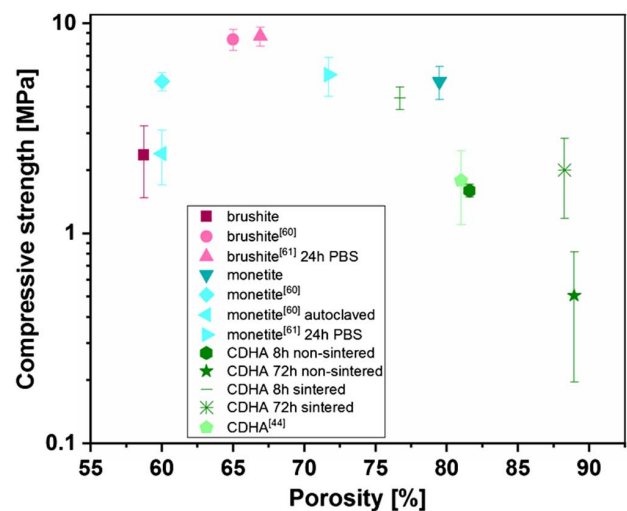

Figure 9. Compressive strength as a function of porosity and comparison with literature values. Compressive strengths determined in the present study for brushite, monetite, and CDHA are shown in dark red, dark turquoise, and dark green, respectively. The values described in the literature[44,60,61] are shown in the corresponding colors in lighter tones.

**ADVANCED
SCIENCE NEWS**

www.advancedsciencenews.com

**ADVANCED
ENGINEERING
MATERIALS**

www.aem-journal.com

has a compressive strength of about 130–210 MPa,[62–64] this is low, but the values fit in the range of trabecular bone, which is between 0.1 and 16 MPa.[63] Thus, it was demonstrated that all samples had sufficient stability to be used in nonload-bearing areas and to be handled during surgery.

4. Experimental Section

Slurry Preparation: Calcium phosphate scaffolds with aligned pore orientation were fabricated by directional freezing and subsequent freeze-drying of slurries. The slurries consisted of α-TCP powder, which was mixed with a 2% (w/w) alginate solution.

α-TCP powder was synthesized in-house by mixing calcium hydrogen phosphate ($CaHPO_4$, J. T. Baker, Fisher Scientific GmbH, Schwerte, Germany) and calcium carbonate ($CaCO_3$, Merck, Darmstadt, Germany) powder in a molar ratio of 2:1 for 1 h. Subsequently, the mixture was sintered for 5 h at 1400 °C. The sinter cake was then mortared, and the powder was sieved to sizes <350 μm. Afterward, grinding was conducted in a planetary ball mill (PM400, Retsch, Haan, Germany) for 4 h at 200 rpm.

The alginate presolution (2% (w/w)) was prepared by dissolving sodium alginate powder ("Protanal LF 10/60FT," FMC Biopolymer, Philadelphia, USA) in ultrapure water under continuous stirring for 1 h. To remove existing air bubbles, the solution was centrifuged ("Mega Star 1.6 R," VWR, Radnor, USA) for 5 min at 20 °C and 4500 rpm. Subsequently, the α-TCP powder and the alginate solution were mixed in a powder-to-liquid ratio of 1 g mL^{-1} on a glass plate using a spatula.

Directional Freezing: Ice-templating of the slurries took place in a custom-built device (for detailed description, see the study by Stuckensen et al.[18]). The core of this unit is a copper block through which coolant flows. On its top there are two Peltier elements (PEs) one above the other. With the help of the cooled copper block, both the heat generated by the PEs and the heat released during the freezing process can be effectively dissipated. The PEs were tempered differently, which resulted in the generation of an external temperature gradient. After the system was in thermal equilibrium, the slurry was transferred to a mold located between the two PEs for structuring.

To examine the morphology by SEM, the porosity by mercury porosimetry, the specific surface area by nitrogen adsorption, and the phase composition by XRD measurements, samples were fabricated in a mold with a diameter of 39 mm and a height of 5 mm. For mechanical compression tests, the cylinders had a diameter and height of 1 cm.

Freeze-Drying and Sintering: After freeze-structuring, the specimens were lyophilized at −57 °C and a maximum of 1 mbar for 24 h using a freeze-dryer ("Alpha 1-2 LDplus," Christ, Osterode am Harz, Germany). Subsequently, two-thirds of all specimens were sintered for 8 h at 1400 °C with a heating rate of 5 °C min^{-1} and a cooling rate of 10 °C min^{-1} ("TC 5050," Arnold Schröder, Flörsheim am Main, Germany).

Further Specimen Treatment: For a phase conversion into nanocrystalline HA, specimens were hydrothermally treated for 3, 5, and 8 h, respectively, in a pressure vessel ("Pressure Cooker BPR 700 BSS," Sage, Düsseldorf, Germany) at 80 kPa gauge pressure and 117 °C. To avoid dissolution, nonsintered samples were put on a grid, placed above the level of demineralized water, while sintered samples had to be treated in 2.5% w/w Na_2HPO_4 solution for phase conversion. For technical reasons, the maximum incubation time at 117 °C was 8 h. For longer treatment durations of 12, 24, 48, and 72 h, a higher temperature and pressure of 175 °C and 800 kPa, a hydrothermal reactor ("4560 MiniReactor 600 mL," Parr Instruments, Moline, USA) was used. Here, both scaffold types were placed on a custom-made aluminum frame above the water level (demineralized water) during the treatment. Afterward, the samples were dried for 24 h at 60 °C.

To convert α-TCP into the low-temperature calcium phosphates monetite and brushite, nonsintered and sintered samples were subjected to acidic treatment. For this purpose, they were immersed twice for 30 s in 10% phosphoric acid solution (orthophosphoric acid, Merck, Darmstadt, Germany) and then dried at room temperature.

Sample Characterization: XRD measurements were performed using a Bragg–Brentano diffractometer ("D8 Advance DaVinci design," Bruker AXS, Karlsruhe, Germany). For this purpose, one specimen per sample type was ground to fine powder, measured using Cu $K_{\alpha,1}$ line with an acceleration voltage of 40 kV, an emission current of 40 mA, a wavelength of $\lambda = 1.5406$ Å, a 2θ range of 10–60°, a step size of 0.02°, and an integration time of 1 s.

The present phases were qualitatively determined using the PDF2 Database and an evaluation tool ("Diffrac.EVA," Bruker AXS, Karlsruhe, Germany). Rietveld refinement of the corresponding crystal structures of α-TCP (ICDD# 290359), β-TCP (ICDD# 90169), CDHA (ICSD# 26204), brushite (ICSD# 16132), and monetite (ICSD# 31046) was used ("Diffrac.TOPAS," Bruker AXS, Karlsruhe, Germany) to determine both the quantitative content and crystallite size of the aforementioned phases.

To investigate morphological changes caused by hydrothermal and acidic treatment, SEM images of the samples were used. For this purpose, one sample per specimen type was broken and fixed with a carbon cement glue ("Leit C Conductive Carbon Cement," PLANO GmbH, Wetzlar, Germany) on SEM specimen holders (Agar Scientific, Stansted, UK) in such a manner that the fractured surfaces could be examined. A high-vacuum coater ("EM ACE600," Leica, Wetzlar, Germany) was used at a current of 35 mA to apply a 6 nm-thick platinum layer to avoid electrical charging of the samples during SEM examination. A field-emission scanning electron microscope ("Crossbeam 340," Zeiss, Jena, Germany) with an acceleration voltage of 2–5 kV was used for image acquisition.

For the quantitative determination of the length of the crystals resulting from the phase transformation by hydrothermal treatment, crystals were measured using an open source image processing software ("ImageJ," Version 2.0.0). This involved 25 measurements for each sample type. The mean value indicates the respective crystal length, while the error corresponds to the standard deviation.

The pore size distribution, relative pore volume, and porosity of the samples were determined by mercury porosimetry ("Pascal 140" and "Pascal 440," Porotec GmbH, Hofheim, Germany). One exemplary sample was measured for each specimen type.

To determine the specific surface area, a volumetric adsorption analyzer ("ASAP 2020" and "ASAP2010," Micromeritics, Norcross, USA) was applied to measure the nitrogen adsorption isotherm at 77 K. Prior to analysis, the samples were degassed at 150 °C for at least 2 h. For each analysis, a mass of about 1.5–2 g was used. The isotherms were evaluated in the relative pressure range below 0.3 with respect to the specific BET surface area using the software "microactive" by the instruments' supplier.

The mechanical properties of the specimens were evaluated by compression strength measurements using a universal testing machine ("Z010," ZwickRoell, Ulm, Germany) equipped with a 10 kN load cell. Sample cylinders were loaded with a force parallel to their longitudinal axis at a test speed of 1 mm min^{-1} until complete failure occurred. With this failure force F and the surface area A of the cylinder, the compressive strength σ was calculated using Equation (4)

$$\sigma = \frac{F}{A} \tag{4}$$

For each sample type, five measurements were performed. The mean value indicates the compressive strength, while the error corresponds to the standard deviation.

Statistical Methods: Statistical analysis was performed using the software "SigmaPlot" (Version 12.5). First, normal distribution of the raw data was proved using the Kolmogorov test. This was followed by applying a one-way ANOVA with post hoc Tukey test. Significant differences are indicated with *($p < 0.05$) and **($p < 0.001$).

Acknowledgements

Conflict of Interest

The authors declare no conflict of interest.

Data Availability Statement

Research data are not shared.

Keywords

[1] S. Weiner, W. Traub, H. D. Wagner, *J Struct. Biol.* 1999, *126*, 241.
[2] M. J. Olszta, X. G. Cheng, S. S. Jee, R. Kumar, Y. Y. Kim, M. J. Kaufman, E. P. Douglas, L. B. Gower, *Mater. Sci. Eng., R* 2007, *58*, 77.
[3] S. Weiner, W. Traub, *FASEB J.* 1992, *6*, 879.
[4] A. Kolk, J. Handschel, W. Drescher, D. Rothamel, F. Kloss, M. Blessmann, M. Heiland, K. D. Wolff, R. Smeets, *J Craniomaxillofac. Surg.* 2012, *40*, 706.
[5] G. Hannink, J. J. C. Arts, *Injury* 2011, *42*, S22.
[6] S. F. Hulbert, *Fed. Proc.* 1970, *30*, A705.
[7] J. J. Campbell, A. Husmann, R. D. Hume, C. J. Watson, R. E. Cameron, *Biomaterials* 2017, *114*, 34.
[8] S. Muehleder, A. Ovsianikov, J. Zipperle, J. Redl, W. Holnthoner, *Front. Bioeng. Biotechnol.* 2014, *2*, 52.
[9] A. P. M. Madrid, S. M. Vrech, M. A. Sanchez, A. P. Rodriguez, *Mater. Sci. Eng. C-Mater.* 2019, *100*, 631.
[10] H. Seitz, U. Deisinger, B. Leukers, R. Detsch, G. Ziegler, *Adv. Eng. Mater.* 2009, *11*, B41.
[11] U. Gbureck, T. Hoelzel, I. Biermann, J. E. Barralet, L. M. Grover, *J. Mater. Sci.-Mater. M* 2008, *19*, 1559.
[12] U. Gbureck, E. Vorndran, F. A. Muller, J. E. Barralet, *J Control Release* 2007, *122*, 173.
[13] P. Habibovic, U. Gbureck, C. J. Doillon, D. C. Bassett, C. A. van Blitterswijk, J. E. Barralet, *Biomaterials* 2008, *29*, 944.
[14] A. Khalyfa, S. Vogt, J. Weisser, G. Grimm, A. Rechtenbach, W. Meyer, M. Schnabelrauch, *J. Mater. Sci.-Mater. M* 2007, *18*, 909.
[15] J. Y. Lee, B. Y. Choi, B. Wu, M. Lee, *Biofabrication* 2013, *5*, 045003.
[16] R. F. Richter, T. Ahlfeld, M. Gelinsky, A. Lode, *Materials* 2019, *12*, 2022.
[17] R. Detsch, F. Uhl, U. Deisinger, G. Ziegler, *J. Mater. Sci.-Mater. M* 2008, *19*, 1491.
[18] K. Stuckensen, A. Schwab, M. Knauer, E. Muinos-Lopez, F. Ehlicke, J. Reboredo, F. Granero-Molto, U. Gbureck, F. Prosper, H. Walles, J. Groll, *Adv. Mater.* 2018, *30*, 1706754.
[19] S. Deville, E. Saiz, R. K. Nalla, A. P. Tomsia, *Science* 2006, *311*, 515.
[20] S. Deville, E. Saiz, A. P. Tomsia, *Biomaterials* 2006, *27*, 5480.
[21] S. Flauder, U. Gbureck, F. A. Muller, *Acta Biomater.* 2014, *10*, 5148.
[22] M. Bohner, *Injury* 2000, *31*, S37.

[23] E. Fernandez, F. J. Gil, M. P. Ginebra, F. C. M. Driessens, J. A. Planell, S. M. Best, *J. Mater. Sci.-Mater. M* 1999, *10*, 169.
[24] F. Tamimi, Z. Sheikh, J. Barralet, *Acta Biomater.* 2012, *8*, 474.
[25] L. Galea, D. Alexeev, M. Bohner, N. Doebelin, A. R. Studart, C. G. Aneziris, T. Graule, *Biomaterials* 2015, *67*, 93.
[26] L. G. Galea, M. Bohner, J. Lemaitre, T. Kohler, R. Muller, *Biomaterials* 2008, *29*, 3400.
[27] H. Monma, T. Kanazawa, *J. Ceram. Soc. Jpn.* 2000, *108*, S75.
[28] E. L. Ritman, *Annu. Rev. Biomed. Eng.* 2011, *13*, 531.
[29] D. M. Stefanescu, R. Ruxanda, in *ASM Handbook Volume 9 – Metallography and Microstructures*, Vol. *9* (Ed.: G. F. V. Voort), ASM International, Materials Park, OH 2004, pp. 71.
[30] H. Shen, E. Y. Yi, M. Amores, L. Cheng, N. Tamura, D. Y. Parkinson, G. Y. Chen, K. Chen, M. Doeff, *J Mater Chem A* 2019, *7*, 20861.
[31] L. Zhang, X. S. Liu, A. Deb, G. Feng, *ACS Sustain. Chem. Eng.* 2019, *7*, 19910.
[32] L. Bahari, A. Bein, V. Yashunsky, I. Braslavsky, *Plos One* 2018, *13*.
[33] U. G. K. Wegst, M. Schecter, A. E. Donius, P. M. Hunger, *Philos. Trans. R Soc. A* 2010, *368*, 2099.
[34] H. Bai, Y. Chen, B. Delattre, A. P. Tomsia, R. O. Ritchie, *Sci. Adv.* 2015, *1*, e1500849.
[35] H. W. Qu, H. Y. Fu, Z. Y. Han, Y. Sun, *RSC Adv.* 2019, *9*, 26252.
[36] N. Abbasi, S. Hamlet, R. M. Love, N. T. Nguyen, *J. Sci.-Adv. Mater. Dev.* 2020, *5*, 1.
[37] T. W. Kim, S. C. Ryu, B. K. Kim, S. Y. Yoon, H. C. Park, *Met. Mater. Int.* 2014, *20*, 135.
[38] J. H. Kim, J. H. Lee, T. Y. Yang, S. Y. Yoon, B. K. Kim, H. C. Park, *Ceram. Int.* 2011, *37*, 2317.
[39] Q. Fu, M. N. Rahaman, F. Dogan, B. S. Bal, *J. Biomed. Mater. Res. B* 2008, *86b*, 514.
[40] N. Monmaturapoj, W. Soodsawang, W. Thepsuwan, *J. Porous Mater.* 2012, *19*, 441.
[41] L. C. Chow, *Monogr. Oral Sci.* 2001, *18*, 148.
[42] R. G. Carrodeguas, S. De Aza, *Acta Biomater.* 2011, *7*, 3536.
[43] S. Karashima, A. Takeuchi, S. Matsuya, K. Udoh, K. Koyano, K. Ishikawa, *J. Biomed. Mater. Res. A* 2008, *88a*, 628.
[44] H. Guo, J. C. Su, J. Wei, H. Kong, C. S. Liu, *Acta Biomater.* 2009, *5*, 268.
[45] K. Ioku, G. Kawachi, S. Sasaki, H. Fujimori, S. Goto, *J. Mater. Sci.* 2006, *41*, 1341.
[46] M. Kamitakahara, C. Ohtsuki, G. Kawachi, D. Wang, K. Ioku, *J. Ceram. Soc. Jpn.* 2008, *116*, 6.
[47] J. Y. Rho, L. Kuhn-Spearing, P. Zioupos, *Med. Eng. Phys.* 1998, *20*, 92.
[48] S. Weiner, H. D. Wagner, *Annu. Rev. Mater. Sci.* 1998, *28*, 271.
[49] G. E. Poinern, R. K. Brundavanam, N. Mondinos, Z. T. Jiang, *Ultrason Sonochem* 2009, *16*, 469.
[50] J. E. Barralet, K. J. Lilley, L. M. Grover, D. F. Farrar, C. Ansell, U. Gbureck, *J. Mater. Sci.-Mater. M* 2004, *15*, 407.
[51] R. Kniep, P. Simon, *Top Curr. Chem.* 2007, *270*, 73.
[52] R. Kniep, P. Simon, *Angew. Chem., Int. Ed.* 2008, *47*, 1405.
[53] H. Tlatlik, P. Simon, A. Kawska, D. Zahn, R. Kniep, *Angew. Chem., Int. Ed.* 2006, *45*, 1905.
[54] P. Simon, U. Schwarz, R. Kniep, *J. Mater. Chem.* 2005, *15*, 4992.
[55] C. Gobel, P. Simon, J. Buder, H. Tlatlik, R. Kniep, *J. Mater. Chem.* 2004, *14*, 2225.
[56] D. Apelt, F. Theiss, A. O. El-Warrak, K. Zlinszky, R. Bettschart-Wolfisberger, M. Bohner, S. Matter, J. A. Auer, B. von Rechenberg, *Biomaterials* 2004, *25*, 1439.
[57] A. Oberle, F. Theiss, M. Bohner, J. Muller, S. B. Kastner, C. Frei, K. Zlinszky, S. Wunderlin, J. A. Auer, B. von Rechenberg, *Schweiz Arch Tierh* 2005, *147*, 482.

[58] F. Theiss, D. Apelt, B. A. Brand, A. Kutter, K. Zlinszky, M. Bohner, S. Matter, C. Frei, J. A. Auer, B. von Rechenberg, *Biomaterials* **2005**, *26*, 4383.

[59] F. Abbona, F. Christensson, M. F. Angela, H. E. L. Madsen, *J. Cryst. Growth* **1993**, *131*, 331.

[60] Z. Sheikh, Y. L. Zhang, L. Grover, G. E. Merle, F. Tamimi, J. Barralet, *Acta Biomater.* **2015**, *26*, 338.

[61] F. Tamimi, D. Le Nihouannen, H. Eimar, Z. Sheikh, S. Komarova, J. Barralet, *Acta Biomater.* **2012**, *8*, 3161.

[62] Y. H. An, in *Mechanical Testing of Bone and the Bone-Implant Interface* (Eds.: Y. H. An, R. A. Draughn), CRC Press, Boca Raton **2000**, pp. 41.

[63] L. C. Gerhardt, A. R. Boccaccini, *Materials* **2010**, *3*, 3867.

[64] K. Rezwan, Q. Z. Chen, J. J. Blaker, A. R. Boccaccini, *Biomaterials* **2006**, *27*, 3413.